An Investigation of Weld Cracking in Alloy 800

Hot cracking susceptibility is associated with heat-to-heat variations in silicon and titanium

BY J. C. LIPPOLD

ABSTRACT. The fusion zone hot cracking susceptibility of four commercial heats of alloy 800 was evaluated with the aid of the Varestraint test. The onset of hot cracking along fusion zone grain boundaries was associated with low melting liquid films which formed as a result of titanium, silicon, and niobium partitioning during solidification. These liquid films appeared to wet the boundaries, producing preferential sites for hot crack formation.

Silicon was present in large concentrations, primarily in elemental form, on the hot crack fracture surface. Some proportion of the titanium and almost all the niobium were combined as a (Ti, Nb)-rich carbide precipitated on the fracture surface. The silicon content was found to exert the greatest influence on the hot cracking susceptibility of the four heats which were evaluated.

A mechanism is proposed to describe the hot cracking process in autogenous alloy 800 weldments.

Introduction

Alloy 800 is an iron-based, fully austenitic alloy, which is often selected for use in high temperature environments where a combination of strength and corrosion resistance is required. Two forms of this alloy, designated as 800 and 800H, are commonly available for a variety of these applications.

The 800 grade contains 0.03-0.10 wt-% carbon and is heat treated to produce a fine-grained microstructure interspersed with $M_{23}C_6$ and MC carbides. This version of alloy 800 is used primarily for applications where corrosion resistance is important.

The 800H grade is restricted to higher carbon (0.05-0.10 wt-%) levels and is solution annealed to dissolve the carbides and produce a coarse grained microstructure. Alloy 800H is usually specified in applications which require improved creep rupture properties relative to alloy 800.

Representative microstructures of both the 800 and 800H alloys are shown in Fig. 1.

Weldability

Despite the widespread use of alloys 800 and 800H by both the petrochemical and power generation industries, the welding metallurgy of this alloy system has received little attention in the metallurgical literature. For most applications, alloy 800 is welded using a high nickel filler material such as Inconel 82*, which is specially formulated to minimize hot cracking. However, it is often necessary to perform autogenous (fillerless) welds as in the case of tube-to-header welds or when joining thin sheets.

The reliability of these welds is generally good in comparison to other fully austenitic stainless steels; however, several investigations have reported that isolated heats of material may be susceptible to cracking in either the fusion zone or the terminal weld crater (Refs. 1-4). To date, no unified model has been proposed which can relate the hot cracking susceptibility to heat-to-heat variations in chemical composition.

Registered trademark of the International Nickel Co.

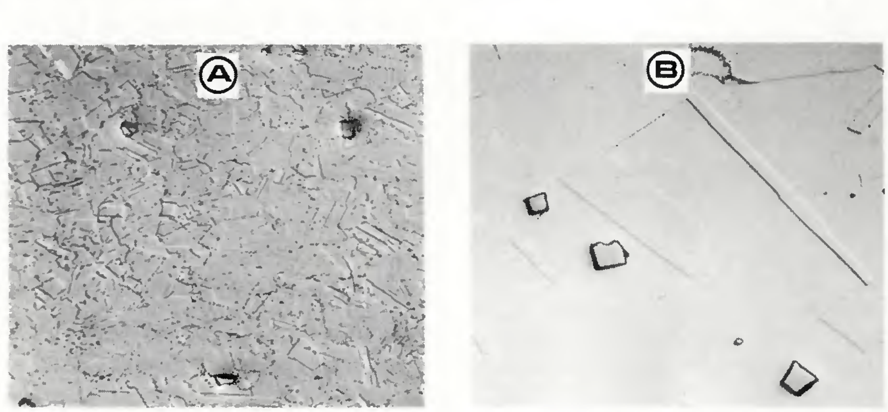

Fig. 1 — Alloy 800 and 800H microstructures: A — 800; B — 800H

J. C. LIPPOLD is with Sandia National Laboratories, Livermore, California.

York and Flury (Ref. 2) proposed that the hot cracking susceptibility of electron beam welds is related to the elemental ratio (Al + Ti)/C + Si), with higher values exhibiting improved resistance to hot cracking. This formulation conflicts with the findings of Canonico *et al.* (Ref. 5), who used the Varestraint test to show that additions of both Ti and Al to a ternary reference alloy increased the hot cracking susceptibility of the alloy system. Varestraint results from tests on commercial heats of alloy 800 showed a further increase in crack susceptibility, suggesting that other alloying or impurity elements may be equally important to the cracking sensitivity of alloy 800 weldments. Neither York and Flury (Ref. 2) nor Canonico *et al.* (Ref. 5) used the analytical techniques needed to determine the extent of elemental partitioning along solidification boundaries.

Wohlstenholme (Ref. 3) has proposed that crater cracking in both autogenous alloy 800 welds and those using an Inconel 82 filler material resulted from the depression of the solidus temperature by the segregation of carbon. Fracture surfaces of the crater cracks were decorated with titanium carbide networks, which formed during the final stages of solidification.

Backman *et al.* (Ref. 6) used the Varestraint test to demonstrate that, when the silicon content is kept low and the manganese content is high, the resistance to hot cracking improves. They proposed that reducing silicon and increasing manganese leads to lower carbon activity and reduces the precipitation of titanium carbide (or carbonitride) in the fusion zone grain boundaries. Also, they suggested that a high manganese content reduces the segregation of silicon during solidification.

In an investigation of HAZ cracking of alloy 800 and 800H (Ref. 7), the author observed large concentrations of titanium and phosphorus in backfilled HAZ cracks. The composition of these backfilled regions reflected the concentration of alloying and impurity elements along fusion zone solidification boundaries. For this reason, it seems likely that both titanium and phosphorus promote the formation of low melting films along these boundaries.

Investigation Objectives

In summary, the results of both hot cracking susceptibility tests and analysis of service failures in alloy 800 and 800H weldments suggest that titanium, aluminum, silicon, manganese, carbon, sulfur, and phosphorus are in some way associated with the incidence of hot cracking in the fusion zone. The purposes of the investigation discussed in this paper were:

1. To identify the elements which contribute to weld hot cracking in alloy 800.
2. To devise a model which explains the role of these elements in the crack formation process.

Table 1—Alloy 800 Chemical Composition, Wt-%[a]

	Heat identification			
	A (HH 7055A)	B (HH 8579A)	D (HH 8989A)	E (HH 9019A)
C	0.06	0.08	0.05	0.07
Mn	0.87	0.93	0.63	0.81
Si	0.39	0.08	0.26	0.15
Ti	0.42	0.49	0.42	0.44
Al	0.19	0.40	0.30	0.47
Cu	0.64	0.71	0.67	0.32
Cr	19.94	19.55	19.88	20.42
Ni	33.95	32.47	31.88	32.83
S	0.003	0.004	0.004	0.003
P	0.01	0.008	0.008	0.008
N	0.020	0.018	0.019	0.017
Nb	0.05	0.05	0.05	0.04
Fe	Bal.	Bal.	Bal.	Bal.

(a) Average of two independent analyses.

Experimental Procedure

Material

The hot cracking susceptibility of four commercial heats of alloy 800 was evaluated in this investigation. The composition of the four heats is listed in Table 1.

The as-received material was in the form of bar stock which had been mill-annealed at 980°C (1800°F). The mill-annealing heat treatment resulted in the fine-grained austenitic microstructure shown in Fig. 1A.

Varestraint Test

The Varestraint test (Ref. 8) was employed to determine the relative hot cracking susceptibility of the commercial alloys. Varestraint test bars—each 15 × 2.5 × 0.65 cm (6.0 × 1.0 × 0.25 in.)—were machined from the bar stock with the 15 cm (6.0 in.) dimension parallel to the rolling direction of the bar. Samples were tested in the Varestraint apparatus over a range of augmented strains from 0.5 to 3.0%. The augmented strain, ϵ, is given by the following relationship:

$$\epsilon \cong t/2R$$

where t is the specimen thickness (~6.5 mm, *i.e.*, 0.25 in.) and R is the radius of the die block over which the specimen is bent.

The welding conditions used during the Varestraint test are listed in Table 2. The conditions were selected in order to produce a weld bead approximately 10 mm (0.4 in.) wide. A trailing shielding gas was employed on the GTA torch during the test to minimize oxidation of the region where cracks form and subsequently facilitate the measurement and tabulation of crack length data.

Crack tabulation was performed on the as-welded surface of the specimen with the aid of a binocular microscope equipped with a filar eyepiece. All crack measurements were performed at ×100 magnification.

Metallographic/Analytical Evaluation

Following crack tabulation, selected Varestraint test samples were mounted and metallographically polished through 0.05 μm (0.000002 in.) alumina. Samples were etched with a mixed acid reagent containing equal parts of nitric, hydrochloric, and acetic acid in order to reveal the microstructural details of the region containing hot cracks. These samples were also subjected to electron microprobe analysis to determine the degree of solute and/or impurity partitioning that is associated with both the solidification and hot cracking phenomena in the fusion zone. The analyses were performed at an accelerating voltage of 25 kV and a beam current of 10 nA, producing an effective probe size of approximately 1 μm (0.00004 in.).

Table 2—Varestraint Test Conditions

Welding current, A	170 ± 10
Welding voltage, V	14 ± 1
Travel speed, mm/s (ipm)	2.55 (6)
Argon shielding gas, L/min (cfh)	14.16 (30)
Electrode to work distance,[a] mm (in.)	2.38 (3/32)
Average weld pool width, mm (in.)	9.5 (0.375)
Augmented strain range, %	0.5 – 3.1

(a)A 2.38 mm (3/32 in.) W-ThO_2 electrode with a 60 deg included angle was used.

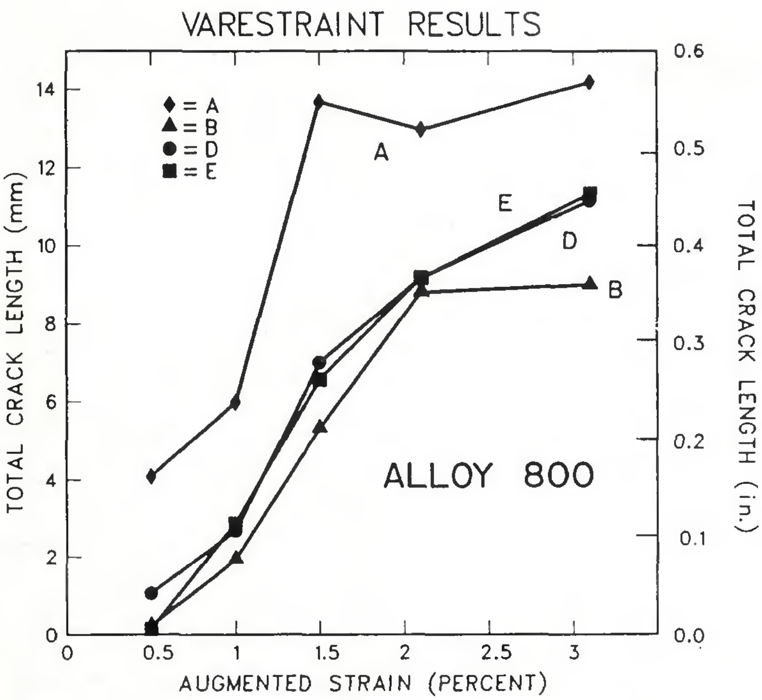

Fig. 2 — Subscale Varestraint test results for four commercial heats of alloy 800

The electron microprobe was also used to identify and differentiate intermetallic particles and/or second phases in the fusion zone. The electron beam scanned several 9000 μm^2 (13.95×10^{-6} in.^{2}) areas and indexed all particles greater than 0.3 μm (0.000012 in.) in the largest dimension. The data were then accumulated and tabulated using a computer program which provided histograms of the particle size distribution.

Varestraint test samples containing hot cracks were also carefully sectioned and broken in order to reveal the hot crack fracture surface. The fracture surfaces were examined through a scanning electron microscope (SEM) equipped with an energy dispersive spectrometer (EDS) detector in order to determine the fracture morphology and identify particles associated with the hot crack surface.

These fracture surfaces were also examined with a scanning Auger microscope in order to evaluate the composition of the near-surface region of the hot crack. An accelerating voltage of 5 kV and a beam current of 0.3 μA were employed. Compositional profiles to a depth of 100 nm (0.000004 in.) below the fracture surface were obtained by sputtering away successive layers of material using a beam of argon ions.

Results

Varestraint Test Results

The number and length of all cracks produced along the trailing edge of the weld pool during the Varestraint test were tabulated at ×100 on the as-welded surface of the sample. The use of a trailing gas shield on the GTA torch throughout the test reduced the oxidation on the surface of the sample and greatly facilitated crack tabulation. Often, when an oxide layer is present on the surface, it is difficult to distinguish cracks in the oxide from actual weld metal cracks.

The results of the Varestraint test plotted as the total length of all cracks on the sample surface versus the augmented tangential strain are shown in Fig. 2 for the four heats of alloy 800. The susceptibility of heats B, D, and E are essentially equivalent and fall in a band below the curve for heat A. The threshold strain level to cause cracking complemented the total crack length results; at the lowest strain level significant cracking was observed in heat A while heats B, D, and E were nearly immune to cracking.

In summary, the Varestraint test results indicated that heat A was considerably more sensitive to hot cracking than the other heats of alloy 800 which were tested.

Metallographic Observations

Following Varestraint testing and crack tabulation, selected samples were mounted for metallographic inspection. The microstructure in the crack-sensitive region of a heat B specimen tested at 3% restraint is shown in Fig. 3.

At low magnification (Fig. 3A), the cracks were observed to emanate radially from a light-etching band which represents the position of the solid-liquid interface at the instant that the sample was bent during the Varestraint test. Note that crack propagation occurred normal to the trailing edge of the weld pool over a distance which corresponds to the brittle temperature range (BTR) of the microstructure.

As defined by Matsuda *et al.* (Ref. 9), the BTR represents the temperature range below the solidus in which liquid films persist along solidification boundaries. Thus, if the BTR increases, the effective crack propagation distance is greater with a subsequent increase in cracking susceptibility as measured by the Varestraint Test.

At higher magnification in Fig. 3B it is evident that crack propagation proceeded intergranularly in the fusion zone. Careful inspection of the microstructure revealed that the growth orientation changes as one moves from one side of the crack to the other. In general, fusion zone grain boundaries (the result of impingement of adjacent subgrains growing in a specific orientation) are preferential sites for crack initiation and propagation.

The as-welded microstructure was fully austenitic and exhibited discrete microconstituents along both grain and subgrain boundaries. An example of the microconstituents commonly observed along the cellular dendritic subgrain boundaries is shown by the SEM micro-

Fig. 3 — Microstructure on the top surface of a heat B Varestraint specimen tested at 3% restraint; arrows indicate the location of the solid-liquid interface when the sample was tested. A — X40; B — X100 (reduced 50% on reproduction)

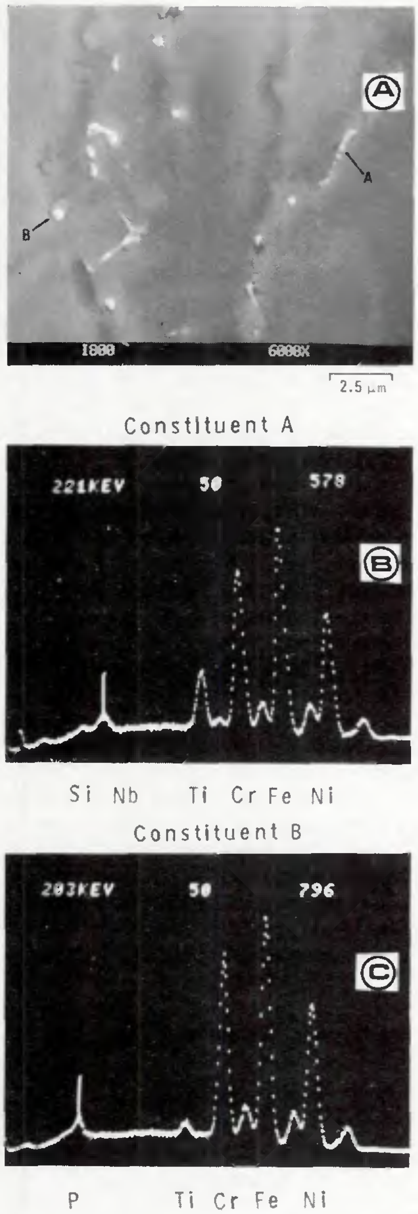

Fig. 4—Fusion zone microconstituents; A—SEM micrograph; B—EDS spectrum from particle A; C—EDS spectrum from particle B

Table 3—Microprobe Particle Identification in Alloy 800

	Particle type	Average Size, μm	No. of particles[a] Heat A	Heat B
Fusion zone	All Types	0.37	662	389
	Ti, Si	0.47	18	3
	P-rich	0.26	—	2
	Ti, P	0.30	4	4
	Cr-Carbide	0.28	112	30
	Ti-Carbide	0.36	448	299
	Mixed Carbide	0.41	64	49
	Large, Ti-Carbide	0.73	16	2
Base metal	All Types	0.21	3551	
	Ti, Si	0.19	8	
	P-rich	—	None	
	Ti, P	—	None	
	Cr-Carbide	0.16	1350	
	Ti-Carbide	0.22	1530	
	Mixed Carbide	0.18	544	
	Large Ti-Carbide	0.87	119	

[a]Average for 9000 μm^2 area

graph in Fig. 4. The EDS spectrum at locations A and B in Fig. 4 revealed that several of the small spherical particles were rich in titanium and phosphorus (particle B), while higher aspect ratio particles, such as the one at point A, were enriched in titanium, niobium, and silicon. The chromium, iron, and nickel peaks arise, in part, from the surrounding matrix in which the particles are imbedded.

The microprobe particle identification program revealed the presence of additional particle types in both the base metal and fusion zone of alloy 800. The results of this identification program are summarized in Table 3. Note that the majority of the particles identified are relatively small Ti- and Cr-rich carbides. Mixed carbides are designated as those which contained both titanium and chromium, while the large Ti-carbides represent the large, blocky particles shown in Fig. 1.

The heat A fusion zone exhibited a higher particle density relative to heat B and also contained a large number of Ti, Si-rich particles. By comparison, the base metal microstructure of heat B exhibited nearly an order of magnitude increase in particle density relative to the fusion zone, suggesting that the carbides are redissolved during the melting process and have little time to precipitate upon cooling from the solidification range.

In general, the fusion zone carbides, which form along the solidification substructure boundaries, are slightly coarser than the similar particle-type in the base metal.

Microsegregation of Alloying Elements

The degree of partitioning of alloying elements during solidification of alloy 800 fusion welds was determined with the aid of the electron microprobe. A microprobe trace made in 1 μm (0.00004 in.) steps across two cell (or cellular dendrite) boundaries is presented in Fig. 5. Although there is little variation in the major alloying additions (chromium and nickel), the cell boundaries are enriched in manganese, titanium, silicon, and niobium relative to the intracellular regions. The aluminum concentration is relatively constant throughout the weld microstructure.

The localized enrichment in niobium was somewhat surprising, since alloy 800 nominally contains only trace amounts of this element. Note that the compositional peaks in Fig. 5 are abrupt, occurring over 3-4 microns (0.0012-0.0016 in.); they represent enrichment along subgrain boundaries rather than at the grain boundaries where hot cracking was observed. The microprobe data in Fig. 5 were gathered from a weld sample from heat A but are representative of the partitioning observed in the other heats.

Crack Backfilling

When the specimen is bent during the Varestraint test, hot cracks initiate at the solid-liquid interface and propagate away from this interface along fusion zone grain boundaries. As the crack opens, liquid from the molten pool immediately in advance of the solid-liquid interface may be drawn into the crack by capillary action. The liquid then solidifies within the confines of the crack and is often concentrated in the crack tip region farthest from the solid-liquid interface.

The composition of the liquid in contact with solid along the trailing edge of the weld pool is either enriched or depleted in solute as a consequence of microscopic equilibrium, which must be maintained at the moving solid-liquid interface. As a result, the composition of the backfilled liquid is indicative of the solute and/or impurity elements which serve to locally reduce the solidification temperature range along grain and subgrain boundaries.

The microstructure in the crack tip region of a heat E Varestraint test specimen is shown in Fig. 6. A continuous dark-etching constituent can be observed at the crack tip (arrow) and to a lesser extent along grain boundaries surrounding the crack. The continuous nature of this constituent at these sites suggests that significant solute and/or impurity enrichment occurred as a result of either crack backfilling or enhanced partitioning of elements to grain boundaries during solidification. The composition of the crack tip region was determined by microprobe analysis of the

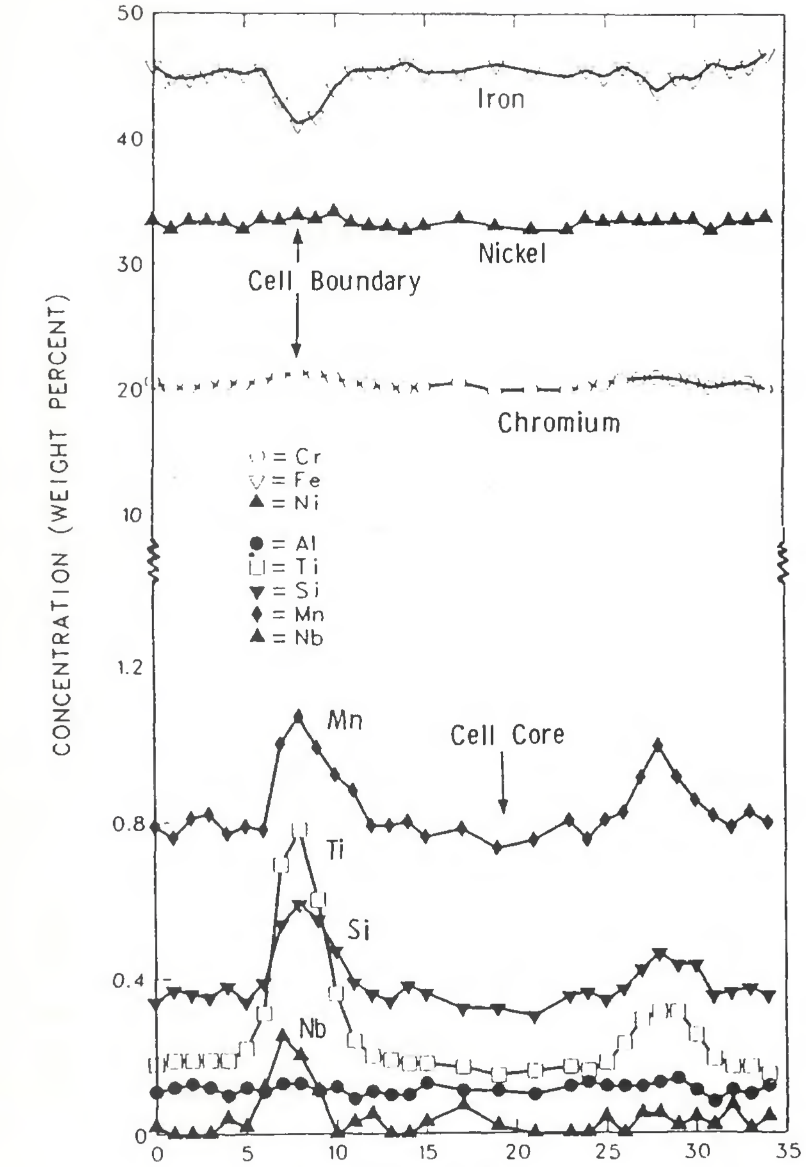

Fig. 5 — Microprobe profile across two cell boundaries in the fusion zone

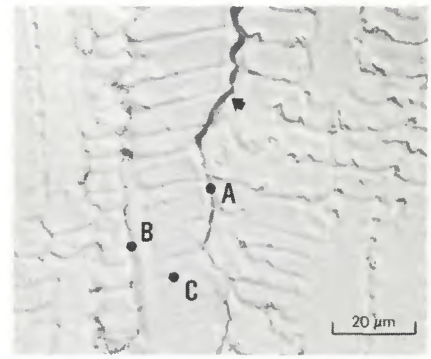

Composition (wt.%)

	A	B	C	Nominal
Al	0.12	0.13	0.10	0.19
Ti	3.79	0.78	0.18	0.42
Cr	20.72	21.37	20.16	19.94
Fe	35.37	41.22	46.15	Bal.
Ni	29.99	33.89	32.67	33.95
Cu	0.73	0.73	0.61	0.64
Si	0.67	0.59	0.38	0.39
Mn	1.18	1.07	0.80	0.87
S	0.01	0.01	0.00	0.003
P	0.03	0.10	0.02	0.01
Nb	1.32	0.20	0.00	--

Fig. 7 — Microprobe analysis of crack tip region. Point A is at the crack tip, point B is along a cellular dendrite boundary, and point C is near the core of the cellular dendrite

Varestraint test samples.

A typical analysis region from a heat A sample tested at 3% restraint is shown in Fig. 7. Point A represents a backfilled boundary at the crack tip, point B represents an adjacent subgrain boundary, and point C is located near the core of the subgrain. The composition of the crack tip region (A) is consistent with the concentration of elements along the solidification subgrain boundaries (B) although, in general, the partitioning is enhanced at the crack tip. The concentrations of titanium and niobium were particularly high at point A relative to both points B and C and the nominal alloy composition.

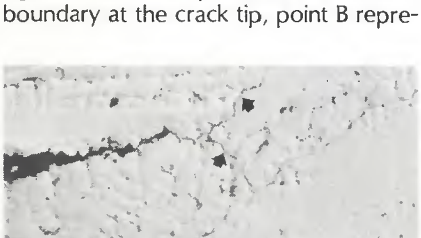

Fig. 6 — Microstructure near the tip of a crack in a heat E Varestraint specimen; note continuous dark-etching constituent at the crack tip and along the grain boundaries. X500 (reduced 40% on reproduction)

SEM Analysis

In order to verify the nature of the cracking process and provide samples for surface composition analysis, regions of the Varestraint test samples containing cracks were carefully sectioned and then fractured to reveal the hot crack surfaces.

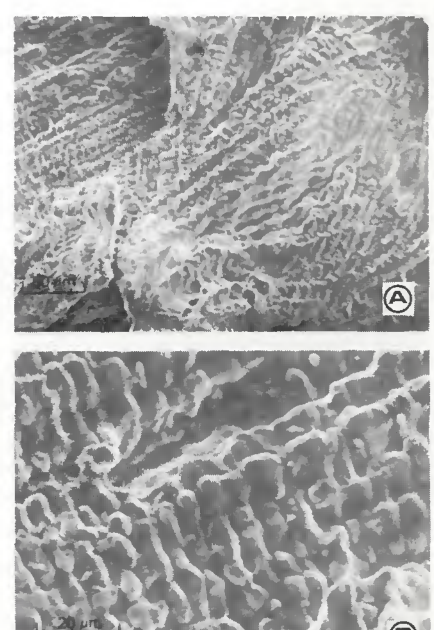

Fig. B — SEM fractograph of a heat E Varestraint hot crack surface. A — X300; B — X1000 (reduced 45% on reproduction)

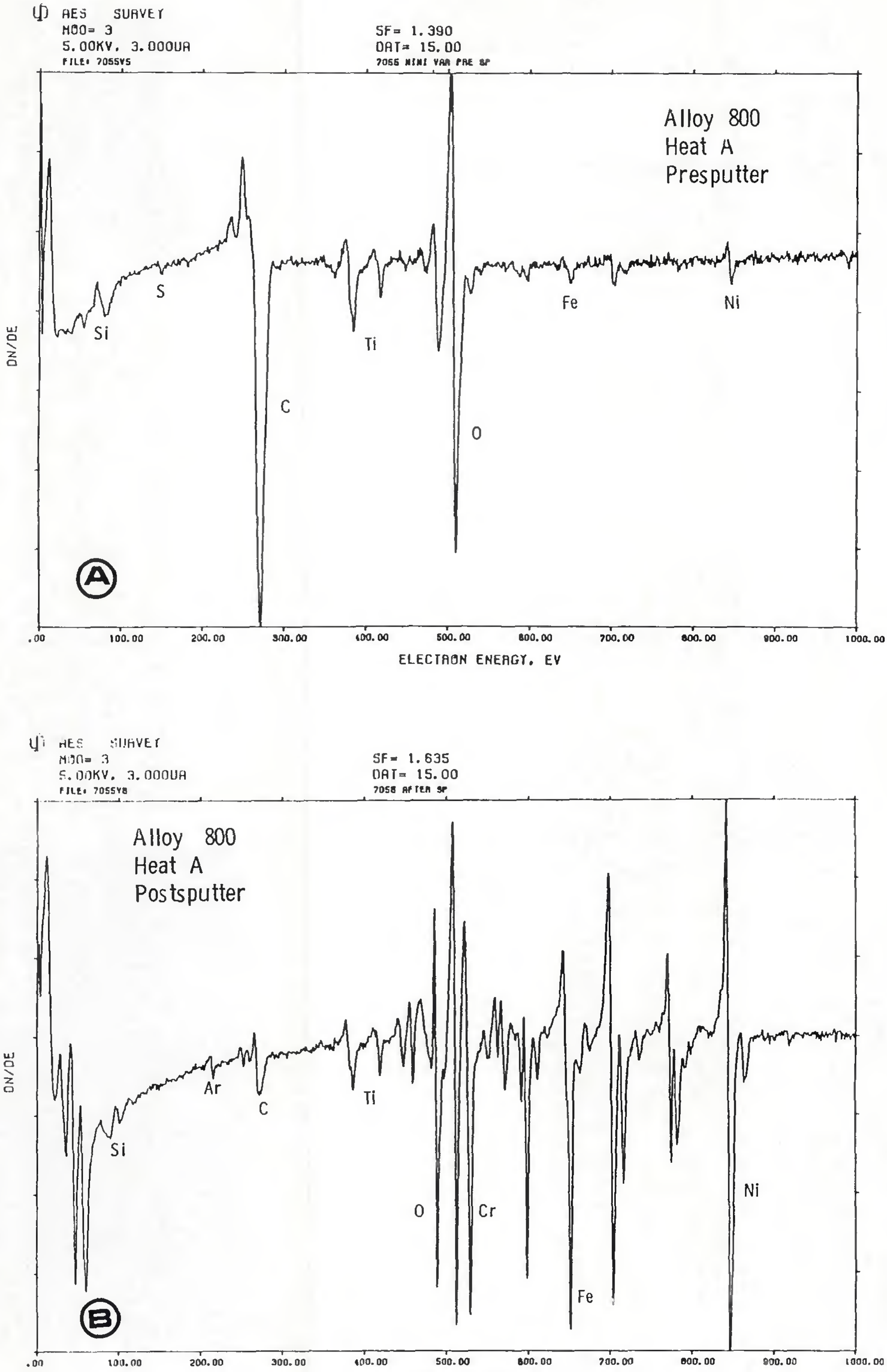

Fig. 9—Auger analysis of heat A hot crack surface; A—pre-sputter; B—after sputtering 100 nm (0.00004 in.) below the crack surface

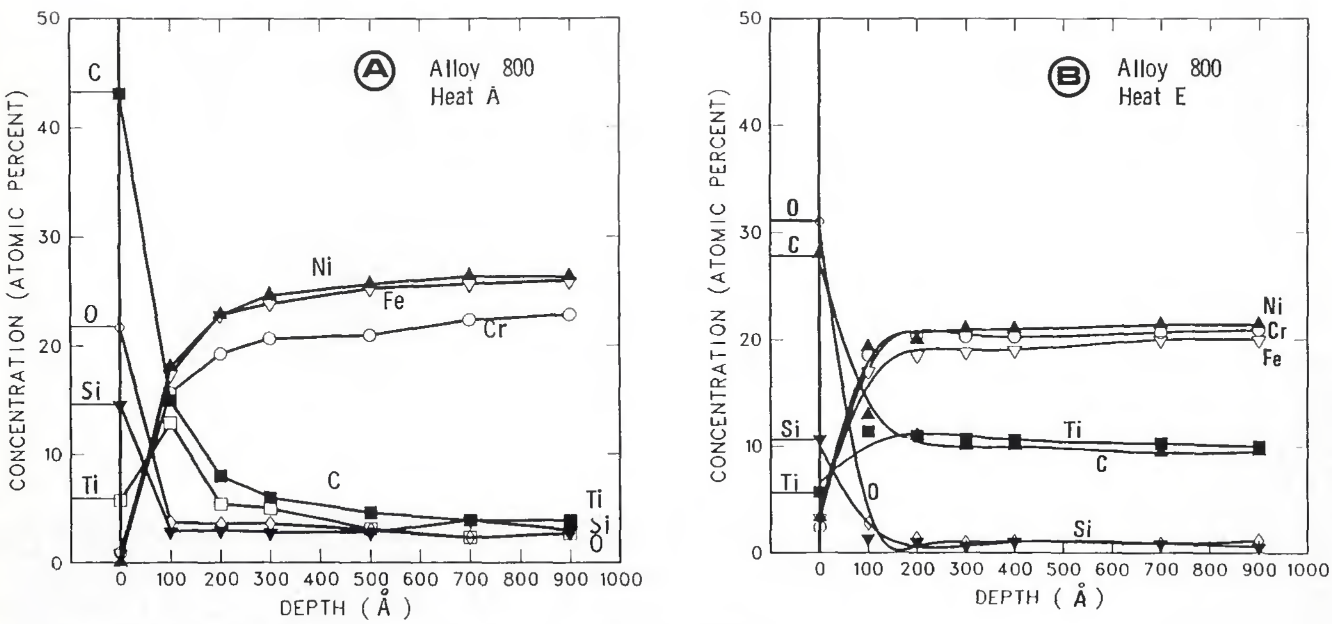

Fig. 10 — Compositional depth profile of a hot crack surface: A — heat A; B — heat E

A typical fracture surface is shown in Fig. 8. The dendritic morphology of the fracture is representative of solidification cracking which is observed in both welds and castings. The periodicity of the peaks and valleys on the fracture surface correspond to the spacing between secondary dendrite arms. Thus, it can be concluded that cracking in the Varestraint test samples occurred during the final stages of solidification and was not the result of a solid-state fracture process.

Auger Surface Analysis

Surface chemistry analysis was performed on the hot crack surfaces of all the heats evaluated by the Varestraint test. The Auger analysis results for a heat A fracture surface plotted as the derivative of the ratio of Auger events to energy (dn/dE) vs. the Auger electron energy are presented in Fig. 9A. Note that the primary elements iron and nickel were nearly absent, but that the surface was highly enriched in silicon and titanium. The large carbon peak resulted from surface contamination, which occurred prior to insertion of the sample into the Auger chamber; the oxygen peak resulted from both contamination and oxidation of the fracture surface during cooling from the solidification range. The use of the inert trailing gas shield was not successful in completely eliminating oxidation of the sample.

In order to remove the oxidation/contamination layer on the fracture surface, a beam of argon ions was used to sputter successive layers of material from the surface. An analysis performed after sputtering nearly 100 nm (3.9×10^{-6} in.) from the fracture surface is shown in Fig. 9B. As can be seen, the levels of iron, chromium, and nickel increased dramatically, while the titanium and silicon levels remained nearly constant. The sharp decrease in the height of the carbon peak suggests that the high surface concentration of carbon was the result of contamination. The argon peak is an artifact of the ion sputtering process.

If the Auger analysis and ion sputtering are performed simultaneously, a compositional depth profile from the surface to a point 100 nm (3.9×10^{-6} in.) below the surface can be obtained. Two such profiles obtained for heat A and heat E hot crack surfaces are shown in Fig. 10. In both cases the surface concentrations of oxygen and carbon were high but dropped off rapidly in the first 20 nm (7.8×10^{-7} in.), while the concentration of iron, chromium and nickel rose to near-nominal levels. The titanium level remains relatively constant throughout the surface layer and parallels the carbon profile below the 20 nm (7.8×10^{-7} in.) contamination layer, suggesting that titanium may be present as TiC. Silicon, which is initially high at the surface, levels off after 10 nm (3.9×10^{-7} in.) and also remains constant throughout the profile. The level of other alloying and impurity elements was either extremely low or undetectable in the surface analysis.

Discussion

Hot cracking in alloy 800 Varestraint test specimens was restricted to fusion zone grain boundaries; it was found to be associated with the segregation of titanium, silicon, niobium, phosphorus, and possibly carbon along these boundaries. Microprobe data presented in Fig. 5 revealed that titanium, silicon, manganese, and niobium partition to cellular dendritic subgrain boundaries during weld solidification.

The partitioning of these elements along fusion zone grain boundaries is even more pronounced due to the impingement of solute-enriched liquid boundary layers, which form in advance of the solid-liquid interface. This impingement can be treated as a macrosegregation phenomenon in contrast to the microsegregation which occurs along the subgrain boundaries. As a result, the concentration of partitioning elements is higher along the grain boundaries and thus promotes the formation of cracks at these sites rather than along the subgrain boundaries.

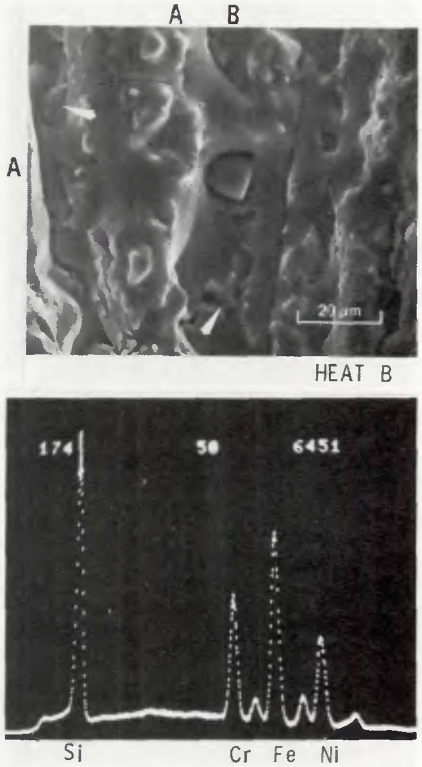

Fig. 11—Fractograph of heat B hot crack surface showing a silicon-rich region at point A-A and an entrapped TiC precipitate at A-B

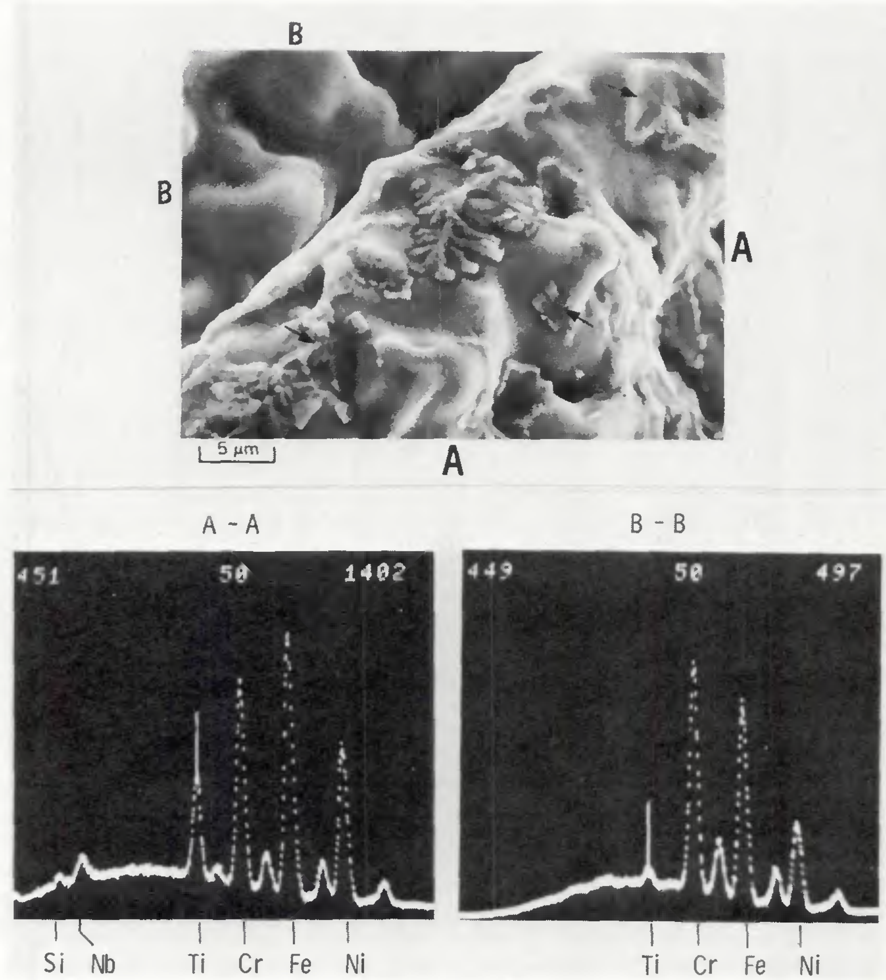

Fig. 12—Fractograph of heat A hot crack surface showing (Ti, Nb)C dendrites superimposed on underlying dendritic structure

Fracture Surface Microconstituents

Since hot cracking occurs preferentially along fusion zone grain boundaries, the hot crack fracture surface represents a planar, or two-dimensional, projection of the one-dimensional boundary observed metallographically. Analysis of this surface using both the SEM and Auger microscope provides a unique opportunity to study the two-dimensional nature of the boundary. Since the fusion zone boundary is formed by the impingement of adjacent cellular dendrites of different growth orientations along a plane roughly perpendicular to the trailing edge of the weld pool, the surface of a crack along this plane reflects the cellular dendritic growth mode as illustrated in Fig. 8. Careful inspection of these surfaces revealed the presence of several distinct microconstituents.

The nature of these constituents is evident in the fractographs of Figs. 11 and 12. Small angular particles located at A-A in Fig. 11 were observed infrequently on the fracture surface. The spectrum obtained with the EDS detector revealed that these particles were rich in silicon. In general, these Si-rich particles were less than 5 microns (0.002 in.) in the longest dimension. Large, blocky titanium carbides (carbonitrides) were also located randomly on the fracture surface as evidenced by the particle at A-B in Fig. 11. These particles were 5–10 microns (0.002–0.004 in.) in size and resulted from the entrapment of the large base metal carbides along grain and subgrain boundaries during solidification. The frequency of these two particle types is consistent with the particle density data presented previously in Table 3.

A third type of microconstituent (indicated by the arrows in Fig. 11 and shown at higher magnification in Fig. 12) exhibited a "feathery" dendrite appearance. The dendritic microconstituent was superimposed on the fracture surface and appeared to have precipitated on the hot crack surface substrate. EDS analysis at point A-A in Fig. 12 revealed that the constituent is titanium-rich relative to an adjacent point at the tip of a secondary arm of the cellular dendrite (point B-B). The morphology of this constituent is similar to the titanium carbide dendrites identified by Wolstenholme (Ref. 3) on the crater crack surfaces of both autogenous welds in alloy 800 and composite welds using IN-82 filler material.

This similarity suggests that some fraction of the titanium, which segregates to fusion zone grain boundaries, is combined as titanium carbide, although the EDS spectrum at point B-B in Fig. 12 shows that some "free" titanium is also present. The spectrum at A-A in Fig. 12 also indicates that niobium and, to a lesser degree, silicon are associated with the microconstituent.

The presence of these elements in addition to titanium supports the results of the microprobe and Auger analysis presented in Figs. 7 and 10, respectively. These particles also represent the Ti-rich carbides identified by the microprobe and reported in Table 3. Note the similarity between the EDS spectrum at point A-A in Fig. 12 and that at point A in Figure 4; it suggests that in a metallographic section the "feathery" carbide appears as a high aspect ratio particle along solidification boundaries.

Hot Cracking Mechanism

Several theories have been proposed to explain the solidification crack suscep-

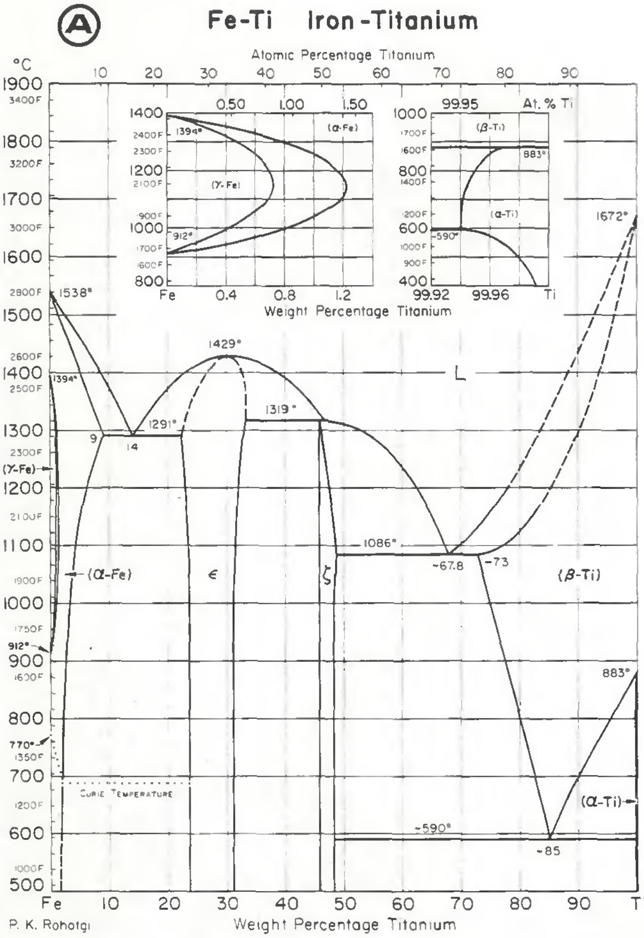

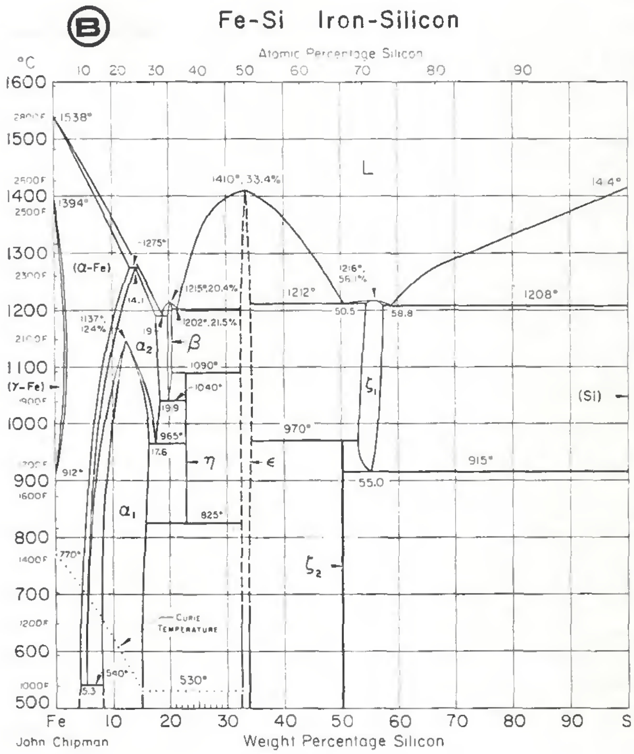

Fig. 13 — Equilibrium phase diagrams: A — Fe-Ti; B — Fe-Si

tibility of alloy 800. Unfortunately, these theories are not in agreement and, in some instances, use similar observations to propose different mechanisms. For example, Wohlstenholme (Ref. 3) hypothesized that an increase in titanium along solidification boundaries would reduce cracking by promoting the precipitation of titanium carbide, thereby mitigating the influence of both elements. In contrast, Backman *et al.* (Ref. 6) suggested that reducing the carbon activity improves the hot cracking resistance by preventing excessive TiC/Ti(C,N) along solidification boundaries. Backman also proposed that the Mn:Si ratio significantly influences the carbon activity and that higher ratios result in improved crack resistance. The ambiguity of these theories is further complicated by the observations of Canonico *et al.* (Ref. 5) and the elemental ratio, (Ti + Al)/C + Si), proposed by York and Flury (Ref. 2).

The detrimental effect of both silicon and niobium on the hot cracking resistance of austenitic stainless steels has been documented in a number of studies (Refs. 4, 10–13). Polgary (Ref. 12) has shown that fully austenitic weld metal is increasingly susceptible to hot cracking as silicon increases in the range from 0.2 to 0.8 wt-%. However, increasing the carbon content at constant silicon concentration reduces the cracking susceptibility. Polgary states that, as the [C]: $\sqrt{[Si]}$ ratio exceeds approximately 0.22, the tendency for cracking in fully austenitic weld metal decreases. At very high carbon contents (>0.20 wt-%), carbide eutectic forms along solidification boundaries and acts to reduce cracking via a phenomenon known as crack healing.

Using Polgary's relationship in conjunction with the compositions listed in Table 1, only heat B exceeded the value of 0.22; this suggested that other elements are also influential with respect to crack susceptibility. The enrichment of titanium along grain boundaries and at the crack tips in Varestraint test samples indicates that this element plays an important role in the hot cracking process.

Inspection of both the Fe-Ti and Fe-Si equilibrium phase diagrams (Ref. 14) shown in Fig. 13 reveals that invariant points occur in the Fe-rich portion of each diagram — a eutectic reaction at 1291°C (2355°F), Fe-14Ti and a peritectic reaction at 1275°C (2327°F), Fe-14.1Si, respectively. Since both these invariant points occur below the bulk solidus temperature (~1375°C, *i.e.,* 2507°F) of alloy 800 (Ref. 15)), segregation of either element along grain and subgrain boundaries will result in a localized depression of the solidification temperature range. Both the microprobe results in Fig. 7 and the Auger results in Figs. 9 and 10 illustrate that the concentration of titanium and silicon in the grain boundary region is very large relative to the bulk composition.

The synergism between titanium and silicon and, in turn, the added effect of phosphorus, niobium and carbon precludes a simple model for hot cracking in alloy 800. Based both on SEM analysis of metallographic structures (Fig. 4) and microprobe analysis of fusion zone particles (Table 3), it appears that phosphorus is combined along subgrain and grain boundaries as a phosphide. The presence of discrete phosphides in the last region to solidify indicates that low-melting phosphorus-rich films do not wet the boundaries and suggest that this impurity is innocuous with respect to the cracking process.

The absence of phosphorus in both the Auger surface analysis and depth profiling results reinforces this hypothesis. The phosphorus enrichment detected by the microprobe along a grain boundary near a crack tip (Fig. 7) probably reflects the presence of a discrete phosphide particle at the analysis point. Sulfur enrichment was also not observed, suggesting that the low (P + S) content of these commercial alloys ameliorates the overall effect of phosphorus and sulfur on the hot cracking susceptibility.

Niobium was also undetectable by Auger analysis. However, it was observed along both subgrain (Fig. 5) and grain (Fig. 8) boundaries by the microprobe. Wolstenholme (Ref. 3) has demonstrated that niobium is combined in the form of (Ti, Nb)C on the surface of alloy 800 crater cracks. Niobium is a potent carbide former; consequently, it appears that nearly all the niobium in the last-to-solidify liquid along the fusion zone grain boundary combines with titanium and carbon to form the feathery precipitates shown in Fig. 12. The inability of the Auger microscope to detect niobium probably results from the random presence of these precipitates on the fracture surface.

The composition of the fracture surface microconstituents and the results of Auger surface analysis indicate that titanium, silicon, niobium, and carbon are enriched along fusion zone grain boundaries and are probably involved to some extent in the mechanism of crack formation. The role of these elements in the hot cracking process can be summarized by the following mechanism.

1. During the final stages of solidification, macroscopic boundaries delineating impinging solidification fronts are enriched in titanium, silicon, and niobium as a consequence of elemental partitioning.

2. The partitioning along these grain boundaries results in a localized depression of the solidus temperature relative to the surrounding microstructure. Since the composition of the liquid at the boundary varies only slightly from that of the bulk, the liquid wets the boundary and forms a nearly continuous film.

3. As the surrounding microstructure cools below the solidification temperature range, thermally-induced stresses and superimposed stress arising from mechanical restraint build up across the boundary. If the liquated boundary is unable to support this stress, as is the case during the Varestraint test, the boundary separates and a crack initiates.

4. As the crack opens, the weld continues to cool and the liquid either freezes along the crack surface or is drawn into the crack tip region by capillary action. As the liquid freezes, the feathery (Ti, Nb)C particles precipitate from the melt and are superimposed on the underlying dendritic morphology of the solidification substructure.

Although manganese was shown to partition to the solidification boundaries (Figs. 5 and 7), it is unclear to what extent manganese participates in the hot cracking mechanism. Mn-rich particles were not observed either on the fracture surface or on a metallographic surface using the microprobe particle identification program.

Several investigators (Refs. 10, 13, 16, 17) have demonstrated the beneficial effect of increased manganese on hot cracking resistance. Generally, manganese must be in the range of 3 to 6 wt-% to significantly affect the crack susceptibility. Since alloy 800 contains on the order of only 1 wt-% Mn, the effect of this element at such low concentrations is probably negligible. In addition, the extremely low sulfur content of these alloys precludes the need to tie up sulfur as MnS. The effect of manganese on carbon activity, as reported by Backman (Ref. 6), may influence the carbide precipitation kinetics during the final stages of solidification.

Both microprobe and Auger results suggest that the partitioning of titanium during solidification and the mobility of carbon via either segregation or diffusion are the important factors influencing the formation of the Ti-rich precipitates along the solidification substructure boundaries. It is likely that niobium accelerates the nucleation kinetics and influences the distribution, and perhaps, the morphology of the precipitates.

Precipitation of (Ti,Nb)C Dendrites

The mechanism by which (Ti,Nb)C dendrites precipitate on the alloy 800 hot crack surface can be described with the aid of the simplified pseudo-binary phase diagram in Fig. 14. The diagram is a schematic representation of the microscopic equilibrium between the metal matrix (M) and some complex carbide (M_xC_y). As liquid of composition C_m (which is situated along fusion zone grain boundaries or on the hot crack surface) cools through the solidification range (M + L), the surrounding liquid becomes increasingly enriched in carbon. Freezing occurs very rapidly and is nonequilibrium in nature; for this reason, solidification will not be completed until some fraction of the liquid reaches the composition of an invariant point such as the eutectic shown at composition C_e in Fig. 14. The final products, which form as a result of the eutectic reaction, will be a mixture of carbide of composition M_xC_y and matrix of composition M_i. The relative proportion of these constituents is a function of the initial composition; as the composition becomes more enriched in carbon (to the right of C_m), the proportion of carbides which form increases.

In the case of alloy 800, the metal matrix will be enriched in titanium and silicon, and the carbide will be of the general form (Ti,Nb)C. As the liquid of eutectic composition solidifies, the carbide phase nucleates on the underlying cellular dendritic substrate and forms the feathery, dendritic precipitate shown previously in Fig. 12.

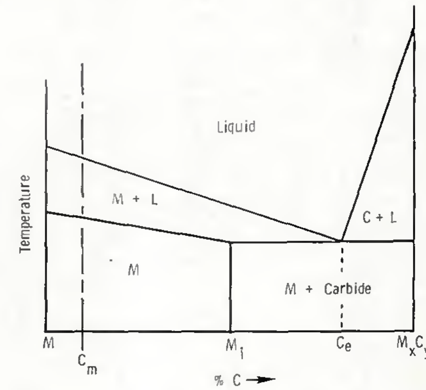

Fig. 14 — Schematic representation of a pseudo-binary phase diagram between a metal matrix and a multi-component carbide

Postweld Sensitization

In an effort to map the location of the titanium in the fusion zone, samples were heat treated at 1000°C (1832°F) for 1 hour (h). Since 1000°C (1832°F) represents the "nose" of the TiC time-temperature precipitation (TTP) curve for alloy 800 (Ref. 18), TiC should readily precipitate during this heat treatment.

The photomicrograph in Fig. 15 illustrates the extent of precipitation which has occurred. The TiC, which appears as the dark-etching constituent in Fig. 15, is nearly continuous along the fusion zone grain boundaries. Since the diffusivity of titanium is relatively low at 1000°C (1832°F) (Ref. 19) and that of carbon is four orders of magnitude greater than titanium at that temperature (Ref. 20), the precipitation of TiC along the boundaries is further proof that titanium partitions to grain and subgrain boundaries during solidification.

The morphology of the intergranular carbide can be seen in greater detail in the SEM micrograph in Fig. 16. Note the dendritic morphology at the bottom of the micrograph (arrows); this is reminiscent of the (Ti,Nb)C dendrites observed on the hot crack fracture surface. It is

Fig. 15 — Carbide precipitation along fusion zone grain boundaries following a postweld heat treatment at 1000°C (1832°F) for 1 h

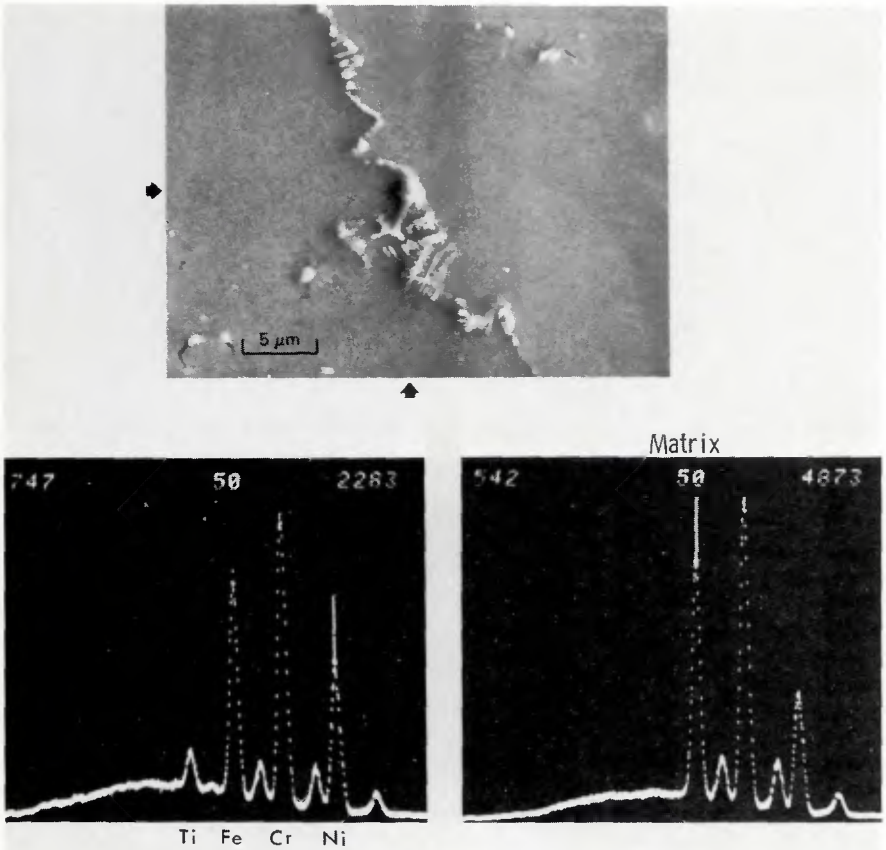

	Boundary	Matrix
Ti/Fe	0.23	-
Cr/Fe	0.83	0.80
Ni/Fe	0.51	0.40

Fig. 16—SEM micrograph of Ti-rich carbide layer along grain boundaries following 1000°C (1832°F) heat treatment for 1 h

likely that these precipitates were present prior to the 1000°C (1832°F) heat treatment.

The high-aspect-ratio precipitates situated along the boundary near the top of the micrograph shown as Fig. 16A are representative of the TiC which has formed during the heat treatment. An EDS spectrum taken at the boundary (Fig. 16B) reveals the titanium enrichment at this point. The adjacent matrix, however, is essentially titanium-free (Fig. 16C) and exhibits only isolated TiC precipitates.

Rationale for Hot Cracking Susceptibility of Alloy 800

The mechanism, which has been proposed to explain the onset of hot cracking in alloy 800, involves the segregation of titanium, silicon, niobium, and carbon to fusion zone grain and subgrain boundaries; it also involves the interaction of these elements along the boundary during the final stages of solidification. The Varestraint test represents a reproducible weldability test which isolates the influence of welding variables and mechanical restraint from heat-to-heat variations in chemical composition.

Reference to Table 1 reveals that the four materials have nearly equivalent titanium concentrations and that the variation in carbon concentration is small. All the materials contained only trace concentrations of niobium. Note, however, that the silicon content of heat A is much greater than that of heats B and E and nearly double that of heat D. Thus (based on the hot cracking mechanism which has been proposed) it appears that, among the four heats of alloy 800 evaluated in this investigation, the difference in silicon content accounts for the variation in hot cracking susceptibility as measured by the Varestraint test.

This conclusion is consistent with the results of Lingenfelter (Ref. 4), who found that a 34Ni-20Cr alloy with 1.25 wt-% Si was far more susceptible to hot cracking than commercial alloy 800. Backman *et al.* (Ref. 6) also suggested that the cracking susceptibility of 30Ni-20Cr alloys could be controlled if the Si content was reduced below 0.25 wt-%.

The detrimental influence of silicon on the hot cracking resistance of alloy 800 weldments is further substantiated by the results of the fractographic and microprobe analyses. Silicon-rich particles were nearly absent on both the fracture surface and the metallographic surface of the materials with low relative crack susceptibility (heats B, D, and E).

Reference to Table 3 reveals a large increase in the number of (Ti, Si)-rich particles when comparing the fusion zone constituents of heats A and B. The increase in Si-rich particle density is further proof of the importance of silicon as a segregant along solidification boundaries where it serves to influence the hot cracking behavior of the alloy.

Despite the increase in particle density, it appears that most of the silicon which partitions to the liquid along the fusion zone grain boundaries remains within the liquid phase rather than forming a precipitate. The Auger results shown previously in Fig. 10 reveal that silicon is present in relatively large concentrations, both at the hot crack surface and to a depth of nearly 100 nm (0.000004 in.) below that surface. The increase in the level of silicon in the crack susceptible heat A sample (Fig. 10A) relative to the heat E sample (Fig. 10B) supports the premise that the silicon content may dictate the hot cracking behavior of the four heats which were evaluated.

Wolstenholme (Ref. 2) has proposed that increasing the titanium content should improve the resistance to hot cracking by controlling the carbon through the precipitation of Ti-rich carbides. In fact, the presence of "free" titanium on the hot crack surface indicates that the titanium is not completely efficient in combining with the carbon. As a result, additional titanium, while possibly serving to tie up more carbon, would undoubtedly increase the "free" titanium in the last liquid to solidify. The tendency for titanium to form a low melting eutectic with Fe-base alloys (Fig. 13) suggests that additional titanium would not reduce the hot cracking susceptibility of alloy 800. This theory is suppported by the results of Canonico *et al* (Ref. 5).

The effect of titanium may be at least as influential as silicon with regards to the cracking susceptibility of alloy 800. Unfortunately, since the titanium concentration of the four heats is nearly equivalent, the relative effect of titanium variations could not be quantitatively assessed. During the course of the investigation, it was observed that the actual titanium concentration of the weld fusion zone was less

Table 4—Elemental Ratios for Predicting Alloy 800 Hot Cracking Susceptibility[a]

Heat	$\frac{Ti + Al}{C + Si}$[b]	$\frac{Ti}{C + Si}$	$\frac{1}{Ti + Si}$	$\frac{Mn}{Ti + Si}$
A	1.34	0.93	1.23	1.07
B	5.6	3.06	1.75	1.63
D	2.3	1.35	1.47	0.93
E	4.1	2.00	1.69	1.37

[a] Lowest number represents greatest susceptibility.
[b] From York and Flury (Ref. 2).

than that of the base material. The reduction in the absolute titanium content resulted from the large, blocky Ti-rich carbides "floating" out of the molten pool during the welding process. These particles were in turn entrapped within a calcium-rich slag which floated on the molten surface and later attached and adhered to the weld metal surface along the trailing edge of the pool.

An SEM micrograph showing the carbides imbedded within the slag is shown in Figure 17A. An optical micrograph taken after the slag was etched away shows the carbides superimposed on the weld surface—Fig. 17B. The fact that titanium and carbon in the form of Ti-rich carbides are removed from the fusion zone during welding tends to mitigate the effect of both these elements on crack susceptibility and increase the importance of silicon in the hot cracking process.

The behavior of carbon during solidification of the fusion zone is nearly impossible to determine using analytical techniques. Wolstenholme (Ref. 3), using the relative potency factor (RPF) of Borland (Ref. 21), predicted that carbon segregates strongly to the liquid during freezing and is primarily responsible for the localized suppression of the solidification temperature range along the dendritic boundaries.

The RPF is based strictly on the shape of the appropriate binary equilibrium phase diagram (Fe-C and Ni-C in this case). It thus cannot accomodate synergistic effects or for example, diffusivity.

In the case of carbon, diffusivity can be quite important. The average diffusion distance of carbon in the austenite at 1350°C (2462°F) is on the order of 10–20 microns (0.0004-0.0008 in.) in 0.1 seconds(s) (Ref. 20).

This distance approximates the primary dendrite arm spacing in alloy 800 welds, and the time is a reasonable estimate of the local solidification time along the dendrite interstices. Consequently, diffusion mitigates the segregation of carbon due to solid-liquid partitioning. As a result the RPF is probably an overestimate of the effect of carbon on the hot cracking susceptibility.

It would appear from the results reported here and those of Wolstenholme (Ref. 3) that some carbon partitioning during solidification must occur. This conclusion is corroborated by the presence of the (Ti,Nb)C precipitates on the hot crack surfaces. In addition, the phenomenon of eutectic healing in alloys containing higher carbon contents suggests that partitioning of carbon contributes to some degree to the formation of liquid films along solidification boundaries in austenitic alloys (Refs. 22, 23). The extensive precipitation of carbide along solidification boundaries following aging (Figs. 15 and 16) demonstrates that not all of the carbon is combined as carbide following weld solidification.

Elemental Ratios

The use of simple elemental ratios to predict weld cracking behavior in complex alloy systems is often confounded by interaction effects among elements and subtle heat-to-heat variations in impurity elements. The elemental ratio used by York and Flury (Ref. 2) has been applied to the four commercial heats evaluated in this study, as presented in Table 4. In addition, three additional relationships based on the results of this investigation and literature information are proposed. Note that the relationship of York and Flury would predict that heat A is more susceptible to cracking than the other heats, although the relative differences in the values do not reflect the results of the Varestraint test—Fig. 2.

The analytical results reported here indicated that aluminum was innocuous with respect to hot cracking susceptibility. Thus the ratio Ti/(C + Si) should be equally as effective as that used by York and Flury. Again, heat A appears the most susceptible, but the spread of values between B, D, and E does not reflect their similar Varestraint results.

A simple inverse of the titanium plus silicon constant (for consistency with the other ratios) again predicts the relative crack susceptibility of heat A and minimizes the spread among B, D, and E. Finally, the reported beneficial effect of Mn is taken into account by the ratio Mn/(Ti + Si). This relationship does not predict the cracking behavior as well as the other three ratios but may be a more appropriate ratio at higher manganese contents (2 wt-%).

A rigorous elemental ratio should also contain a (P + S) factor, since the increase in hot cracking associated with high levels of these impurities is well known. In practice, the impurity content of alloy 800 is kept very low. Thus a simple ratio based on the (Ti + Si) content may suffice for the majority of alloy 800 heats.

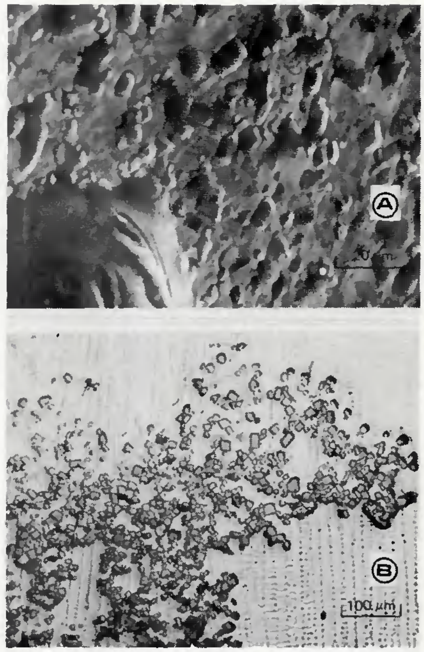

Fig. 17—Weld scale on surface of alloy 800 weldments; cuboidal particles are TiC precipitates which have floated out of the weld pool. A—SEM micrograph, X1000; B—optical micrograph, X150. (A and B reduced 49% on reproduction)

Summary

The subscale Varestraint test was used to determine the relative hot cracking susceptibility of the fusion zone in four commercial heats of alloy 800. Although all four heats were susceptible to cracking, one heat exhibited a significant increase in cracking relative to the other three.

Optical metallography revealed that nearly all the cracking was localized along fusion zone grain boundaries. Microprobe analysis of the grain boundaries detected high concentrations of titanium, silicon, and niobium. The enrichment of these elements along both the grain and subgrain boundaries results from partitioning during solidification and acts to significantly depress the effective solidification temperature range at these sites.

The fusion zone hot cracking mechanism in alloy 800 involves the complex interaction of titanium, silicon, niobium, and carbon along the solidification boundaries. SEM and Auger analyses of the hot crack fracture surfaces revealed the presence of (Ti, Nb)-rich carbides, suggesting that these particles precipitate from the last-to-solidify liquid on the fracture surface. Since the titanium, niobium, and carbon content of the four heats was nearly equivalent, the silicon content had the greatest effect on the hot cracking susceptibility; the heat with the highest silicon content was the most susceptible to fusion zone cracking.

Acknowledgment

The author wishes to thank Richard Bell for the experimental assistance and technical support during the course of this investigation. The work was financially supported by the U.S. Department of Energy, DOE, under contract number DE-AC04-76DP00789.

References

1. King, J. F., and Reed, Jr., R. W. 1976 (Apr.). *Weldability testing of alloy 800.* ORNL report no. TM-7276.

2. York, J. W., and Flury, R. L. 1976 (Feb.). *Assessment of candidate weld metals for joining alloy 800.* Westinghouse Electric Corporation, Tampa Division report #WNET-119 under ORNL contract no. ORNL-4308.

3. Wolstenholme, D. A. 1973. Weld crater cracking in Incoloy 800, *Welding and Metal Fabrication* 41(12):443-449.

4. Lingenfelter, A. C. 1972. Varestraint testing of nickel alloys. *Welding Journal* 52(9):430-s to 436-s.

5. Canonico, D. A., Savage, W. F., Werner, W. J., and Goodwin, G. M. 1969 (July). Effects of minor additions on weldability of Incoloy 800. *Proc. of WRC symposium entitled "Effects of minor elements on the weldability of high-nickel alloys."* New York: Welding Research Council.

6. Backman, A., Ekstrom, U., and Lundquist, B. 1978. The effects of alloying elements and dilution on the hot cracking sensitivity of welds in alloy 800. *DVS Berichti*, no. 52:93-96.

7. Lippold, J. C. 1983. An investigation of heat-affected zone cracking in alloy 800. *Welding Journal* 62(1):1-s to 11-s.

8. Lundin, C. D., and Savage, W. F. 1966. Application of the Varestraint technique to the study of weldability. *Welding Journal* 31(11):497-s to 503-s.

9. Arata, Y., Matsuda, F., and Katayama, S. 1977. Solidification crack susceptibility in weld metals of fully austenitic stainless steels (report II). *Trans. JWRI* 6(1):105-116.

10. Brown, R. S., and Koch, J. B. 1978. Development of a solidification crack resistant weld filler metal for a stabilized fully austenitic alloy. *Welding Journal* 58(2):38-s to 42-s.

11. Moorhead, A. J., and Sikka, V. K. 1979. Effects of residual niobium on Type 304 stainless steel. *Welding Journal* 59(9):253-s to 261-s.

12. Polgary, S. 1969 (Feb.). The influence of silicon content on cracking in austenitic stainless steel with particular reference to 18Cr-8Ni Steel. *Metal Construction:* 93-97.

13. Ogawa, T., and Tsunetomi, E. 1982. Hot cracking susceptibility of austenitic stainless steels. *Welding Journal* 61(3):82-s to 93-s.

14. American Society for Metals. 1973. *Metals Handbook*, 8th ed., vol. 8: 306-307. Columbus, Ohio.

15. Unpublished research performed at Sandia National Laboratories, Livermore, CA, 1981.

16. Honeycombe, J., and Gooch, T. G. 1972 (Dec.). Effect of manganese on cracking and corrosion behavior of fully austenitic stainless steel and weld metal. *Metal Construction and British Welding Journal:* 456-460.

17. Backman, A., and Lundquist, B. 1977. Properties of a fully austenitic stainless steel weld metal for severe corrosion environments. *Welding Journal* 56(1):23-s to 28-s.

18. Allen, R. M., and Jones, W. B. 1982. Mechanical behavior of alloy 800 at 838 K. *Met. Trans* 13A (4):637-648.

19. Swisher, J. H. 1968. Sulfur solubility and internal sulfidation of iron-titanium alloys. *Met. Trans.* 242:2433-2439.

20. Demel, O. 1977. *Radek Rundsch* (2):201-209.

21. Borland, J. C. 1961. *Brit. Weld. Jour.* 8(11):526-540.

22. Cieslak, M. J. 1983. Ph.D Thesis, Rensselaer Polytechnic Institute. Troy, NY.

23. Thomas, Jr., R. D., and Poole, L. K. 1955. Mechanical properties of modified Type 347 weld metals. *Welding Journal* 34(12):583-s to 595-s.

AWS "Peer Review" Panel

The individuals whose names are listed below are participating in the "Peer Review" Program of the American Welding Society as it pertains to the Research Supplement of the *Welding Journal.* Participation consists of evaluating the technical content of papers submitted for publication in the Research Supplement and, to this end, rendering judgments concerning:

- Originality of the contribution.
- Technical value to the welding community.
- Prior publication of the material being reviewed.
- Proper credit to others working in the same technical area.
- Justification of the conclusions judging by the results.
- Degree of acceptability for publication.

It is considered that program participants are rendering an invaluable service to the welding community and to the authors of papers undergoing review. Others wishing to serve as reviewers are asked to contact the Technical Editor of the *Welding Journal,* P.O. Box 351040, Miami, FL 33135.

Current Reviewers

D. K. Aidun
G. A. Andreano
W. R. Apblett Jr.
D. G. Atteridge

W. G. Bader
W. A. Baeslack, III
J. C. Baker
D. J. Ball
C. M. Banas
R. E. Beal
L. S. Beedle
C. R. Behringer
R. Beldyk
W. P. Benter, Jr.
J. T. Biskup
K. L. Brown
A. J. Bryhan

J. M. Cameron
D. A. Canonico
R. S. Chandel
R. A. Chihoski
M. Cieslak
N. S. Cole
C. E. Cross

S. A. David
P. B. Dickerson
D. W. Dickinson
R. D. Dixon
R. B. Dooley
R. J. Dybas

T. W. Eagar
B. J. Eberhard
D. P. Edmonds
G. Edwards
J. W. Elmer

J. W. Fisher
E. A. Flynn
W. R. Frick
E. Friedman
L. M. Friedman

E. B. Gempler
J. M. Gerken
F. E. Gibbs
S. S. Glickstein
G. M. Goodwin
F. J. Grist

J. R. Hannahs
D. W. Harvey
D. C. Helton
R. T. Hemzacek
G. K. Hicken
T. Hikado
J. F. Hinrichs
D. G. Howden
E. I. Husa

J. E. Indacochea

C. E. Jackson
J. J. Jellison
J. E. Jones

P. A. Kammer
W. A. Kawahara
J. F. Key
R. A. Kelsey
J. F. King
W. H. King
G. A. Knorovsky
P. J. Konkol
L. J. Korb
D. J. Kotecki
S. Kou
J. S. Kozelski

F. V. Lawrence, Jr.
G. L. Leone
G. G. Lessmann
D. Link
J. C. Lippold
R. E. Long
C. R. Loper, Jr.
C. D. Lundin
K. A. Lyttle

A. F. Manz

R. P. Martukanitz
K. Masubuchi
D. K. Matlock
S. J. Matthews
R. B. McCauley
J. T. McGrath
H. I. McHenry
E. A. Metzbower
G. E. Metzger
J. A. Miller
J. W. Mitchell
A. J. Moorhead
W. H. Munse
T. M. Mustaleski

T. V. Natale
C. D. Nicky
E. F. Nippes
T. H. North

D. L. Olson
G. W. Oyler

V. J. Papazoglou
B. M. Patchett
D. W. Patterson
R. A. Patterson
A. W. Pense
D. D. Peter
E. Pfender
L. E. Pope
M. Prager

D. D. Rager
K. B. Rao
D. T. Read
W. S. Ricci
R. W. Richardson
G. D. Ries
A. M. Ritter
I. B. Robinson
M. N. Ruoff

E. P. Sadowski
W. W. Sanders, Jr.
L. W. Sandor
S. J. Santangelo
W. F. Savage
J. M. Sawhill, Jr.
M. M. Schwartz
E. G. Shifrin
L. E. Shoemaker
T. A. Siewert
G. M. Slaughter
J. P. Snyder, II
R. E. Somers
D. E. Spindler
J. Spingarn
G. R. Stoeckinger
R. D. Stout
M. A. Streicher
R. D. Sutton

J. R. Terrill
R. D. Thomas, Jr.
C. L. Tsai
A. J. Turner

G. D. Uttrachi

J. J. Vagi
T. L. VanderWert
R. Vasudevan
S. Venkataraman
R. C. Voigt

F. A. Wassell
T. A. Whipple
A. E. Wiehe
W. L. Wilcox
W. L. Winterbottom
C. E. Witherell
J. R. Woodward
K. C. Wu

H. Y. Yoon

H. G. Ziegenfuss